Extending GRMHD for thin disks to non-Kerr spacetimes

Sourabh Nampalliwar[1,2,3,*], Aristomenis I. Yfantis[1,4] and Kostas D. Kokkotas[1]

[1]*Theoretical Astrophysics, IAAT, Eberhard Karls Universität, Tübingen, Germany*
[2]*SISSA, Via Bonomea 265, 34136 Trieste, Italy*
[3]*IFPU—Institute for Fundamental Physics of the Universe, Via Beirut 2, 34014 Trieste, Italy*
[4]*Department of Astrophysics/IMAPP, Radboud University,*
P.O. Box 9010, 6500 GL Nijmegen, Netherlands

Black hole based tests of general relativity have proliferated in recent times with new and improved detectors and telescopes. Modeling of the black hole neighborhood, where most of the radiation carrying strong-field signature originates, is of utmost importance for robust and accurate constraints on possible violations of general relativity. As a first step, this paper presents the extension of general relativistic magnetohydrodynamic simulations of thin accretion disks to parametrically deformed black holes that generalize the Kerr solution. The extension is based on HARMPI, a publicly available member of the HARM family of codes, and uses a phenomenological metric to study parametric deviations away from Kerr. The extended model is used to study the disk structure, stability, and radiative efficiency. We also compute the Fe Kα profiles in simplified scenarios and present an outlook for the future.

I. INTRODUCTION

Tests of theories of gravity in the strong-field regime have become an important field of research in the past few years with the detection of gravitational waves and advances in x-ray spectroscopy, relativistic astrometry, and black hole imaging. While general relativity (GR) has been hugely successful in the weak-field regime [1], its validity in the strong-field regime has recently become testable [2–4], and these tests are expected to get more sensitive in the coming decades.

One of the most remarkable predictions of GR is the existence of black holes (BHs). BHs, being extremely compact, give rise to the strongest gravitational fields in our universe. They can be completely described, at least within GR, with just a few parameters (due to the no-hair theorem [5–8]). Moreover, many of them can be found in our universe, with estimates placing roughly a million of them within our own galaxy [9]. These properties make BHs the ideal candidates for performing strong-field tests of GR.

BH-based tests of gravity in the strong-field regime have become accessible with a variety of observational techniques in recent years. Gravitational waves-based tests began in 2016 [10] (gravitational wave-based tests using pulsar timing have been around for a few decades [11], but these do not probe the strong-field regime as closely as the other listed techniques, see Fig. 2 in Ref. [12]), astrometry-based tests of GR from the center of the Milky Way were

reported in 2018 [4]; in the same year x-rays were first used to probe deviations from GR [13], and BH shadow-based tests were first performed in 2019 [14]. X-ray spectroscopy, in particular, is one of the most interesting and promising techniques in this regard. It is based on the idea of using radiation emanating from and/or traveling close to the BH and thus carrying imprint of its nature. Feasible with both stellar-mass and supermassive BHs alike, with several astrophysical sources already observed, and with relatively cleaner signal than some other techniques, x-ray reflection spectroscopy provides a versatile, independent and complimentary tool to study theories of gravity.

When performing strong-field tests, the immediate neighborhood of the BH is an especially important region, since many of the tests are based on analyzing radiation emanating from here. Precise and accurate tests are, therefore, predicated on precise and accurate modelling of the BH neighborhood. Such modeling is, however, fraught with difficulties. The first serious difficulty is the handling of the alternative theory and the black hole metric being tested, the latter of which can have a complex numerical, or even unknown, form. The second serious difficulty is the handling of complex partial differential equations describing the intermixing of gravitational, electromagnetic and kinetic effects in the BH neighborhood, manifesting even for GR and around Kerr BHs.

In light of the above difficulties in modeling the BH neighborhood, recent years have seen attempts to constrain alternative theories of gravity and possible violations of GR using the approach of decreased fidelity: most of these studies are based on idealistic models of the BH

*Corresponding author.
sourabh.nampalliwar@uni-tuebingen.de

neighborhood, assuming, for instance, an infinitesimally thin accretion disk, perfectly circular orbits for the accreting matter, and so on. There are two major pitfalls with this approach. First, it leads to the introduction of extra parameters in the model, which gives rise to irreducible degeneracies (for instance, between the disk's inner edge and spin, a consequence of the assumption that the disk's inner edge lies at the innermost stable circular orbit (ISCO) [15]). Second, these studies rely on the fundamental assumption that theoretical models of the BH neighborhood, developed assuming the validity of, or compatibility with, GR (for instance, stability of an infinitesimally thin equatorial disk [16]), continue to remain valid in non-GR scenarios that these studies set out to investigate. This makes the whole analysis, at best, unreliable and, at worst, misleading. It is, therefore, imperative to evolve the models of BH neighborhoods in non-GR scenarios to a robust, accurate and reliable framework that can be used to perform accurate tests of GR.

The most promising approach to achieve high-fidelity modeling of the BH neighborhood is magnetohydrodynamic (MHD) simulations. Significant progress has been made in this regard within GR. GRMHD simulations solve coupled systems of partial differential equations comprising of magnetohydrodynamic equations and gravitational field equations. In generic settings (e.g., when simulating gravitational collapse into a BH), one needs to evolve both the *fluid* and the *background* gravitational field. However, accretion of matter can often be modeled in a relatively simpler manner by treating the background field as fixed.[1] These *test-fluid* GRMHD simulations have successfully been applied to diverse astrophysical scenarios, especially when combined with high-resolution shock-capturing (HRSC) techniques. (See Ref. [17] for other techniques like artificial viscosity, smooth particle hydrodynamics, etc.) One of the most popular test-fluid HRSC GRMHD codes in the market today is HARM [18,19]. It uses an energy-conservative method to solve equations of ideal MHD in the Kerr-Schild coordinates. Various extensions of HARM have been developed, to handle three spatial dimensions [20], parallelization [21], M1 radiation closure [22], GPU-acceleration [23], and so on. Another popular choice is the *black hole accretion code* (BHAC) [24]. It uses adaptive mesh refinement techniques to efficiently model the neighborhood, and has been used to simulate images of non-GR BHs [25,26].

Modeling of the BH itself can be approached in two ways. In the first approach, one begins with a specific alternative theory of gravity and uses the BH solutions of that particular theory. In the second approach, one begins with a generic metric and parametrizes it relative to the Kerr metric (often by imposing one or more symmetries that the Kerr metric possesses). Each approach has its advantages and disadvantages. While using a theory-specific metric provides a direct handle on the validity of a physical theory, finding BH solutions in alternative theories of gravity, as in GR, can be extremely difficult. Writing the solution in a form that is convenient for computation adds to the complication. Theory-agnostic metrics can often be written down in a relatively convenient form, but do not have a physical theory behind them and can be difficult to interpret. They can, however, be used without reservation for *null* tests of GR, where parametrized deviations from the BH solutions of GR (often the rotating one known as the Kerr solution [27]) provide a handle on violations of GR via the no-hair theorem.

Within the simplifying assumptions (infinitesimally thin disk with matter in circular orbits, etc. [28]), some of us have developed a framework, RELXILL_NK, to test alternative BHs (of both theory-specific and theory-agnostic types) using x-rays [28,29]. RELXILL_NK has been used to test for deviations from the Kerr solution in both stellar-mass [3,30–32] and supermassive BHs [13,33–36], and it has provided some of the best constraints so far on such deviations. In this work, we take this framework forward and describe our first step toward high-fidelity tests of gravity using x-ray reflection spectroscopy. We present our attempt to model the neighborhood of a non-GR BH described by a theory-agnostic metric using the public, parallelized three-dimensional version of HARM, namely, HARMPI [21]. We mostly perform the simulations in two dimensions (radial and polar, assuming symmetry in the azimuthal direction) due to limitations on computational cost, but show one 3D simulation to illustrate that the qualitative results from 2D simulations hold. This simplified case serves as a stepping stone toward our ultimate goal of high-fidelity modeling of the BH neighborhood. We focus on thin disks, i.e., disks with the Eddington accretion rate in the range 0.1–0.3, since x-ray reflection spectroscopy has primarily been used for such systems and numerical simulations in GR have shown good agreement with models used for data analysis (which use analytic infinitesimally-thin disks). We evolve the classic tori profiles described in Ref. [37] and calculate several properties of the final disk related to stability and radiation. In particular, we compute the iron line profile for MHD-modeled systems and compare them with those for analytic thin-disk systems, finding good agreement.

The rest of the paper is organized as follows. Section II presents a review of the theory-agnostic metric used to model the BH, and HARMPI. In Sec. III, we describe our enhancements to HARMPI. Simulation details are given in Sec. IV. In Sec. V we present the results ranging from disk structure and stability to radiative efficiency and spectrum. We end with Sec. VI with an outlook for the future. In what follows, greek letters are used for spacetime indices, and

---

[1]This can also be understood by realizing that the accretion rate is so small that the mass, and other parameters of the BH, do not change significantly over the timescale of the evolution.

roman for purely spatial indices. The signature of the metric is $(-+++)$ and geometrized units are used such that $G = c = 1$.

II. REVIEW

A. Johannsen metric

One of the most popular choices of theory-agnostic non-Kerr metrics is the one proposed in Ref. [38] (Johannsen metric hereafter). It preserves the separability of Hamilton-Jacobi equations of the Kerr solution (which leads to the existence of a constant of motion, known as the Carter constant in the Kerr case [39], and can be traced back to the conservation of the Killing-Yano tensor [40]) while introducing four new radial functions that quantify the deviation of the metric from Kerr. In Boyer-Lindquist coordinates, the metric components are given as [38]

$$g_{tt}^{\text{BL}} = -\frac{\tilde{\Sigma}(\Delta - a^2 A_2^2 \sin^2\theta)}{B^2},$$

$$g_{t\phi}^{\text{BL}} = -\frac{2a\tilde{\Sigma}\sin^2\theta}{B^2}[(r^2 + a^2)A_1 A_2 - \Delta],$$

$$g_{rr}^{\text{BL}} = \frac{\tilde{\Sigma}}{\Delta A_5},$$

$$g_{\theta\theta}^{\text{BL}} = \tilde{\Sigma},$$

$$g_{\phi\phi}^{\text{BL}} = \frac{\tilde{\Sigma}\sin^2\theta}{B^2}[(r^2 + a^2)^2 A_1^2 - a^2\Delta\sin^2\theta],$$

where the superscript BL indicates that the components are given in Boyer-Lindquist coordinates, M is the BH mass, $a = J/M$ is the BH spin,

$$B = (r^2 + a^2)A_1 - a^2 A_2 \sin^2\theta, \qquad \tilde{\Sigma} = \Sigma + f,$$
$$\Sigma = r^2 + a^2\cos^2\theta, \qquad \Delta = r^2 - 2Mr + a^2,$$

and $\{f, A_1, A_2, A_5\}$ are the four deviation functions. The deviation functions are written in terms of power series over M/r, and after setting the lower order coefficients, dictating far-field behavior of the spacetime, to their GR values, and retaining the leading order parameters that dictate near-field behavior of the spacetime, we get

$$f = \epsilon_3 \frac{M^3}{r}, \qquad A_1 = 1 + \alpha_{13}\left(\frac{M}{r}\right)^3,$$

$$A_2 = 1 + \alpha_{22}\left(\frac{M}{r}\right)^2, \qquad A_5 = 1 + \alpha_{52}\left(\frac{M}{r}\right)^2.$$

Here, ϵ_3, α_{13}, α_{22}, and α_{52} are the leading order deviation parameters and are dimensionless. The metric reduces to the Kerr metric for $\epsilon_3 = \alpha_{13} = \alpha_{22} = \alpha_{52} = 0$.

Since the HARM family of codes also require the metric in horizon-penetrating coordinates, we use the above metric in Kerr-Schild-like coordinates, also given in Ref. [38]:

$$g_{tt}^{\text{KS}} = -\frac{\tilde{\Sigma}[\Delta - a^2 A_2(r)^2\sin^2\theta]}{F},$$

$$g_{tr}^{\text{KS}} = \frac{\tilde{\Sigma}}{\sqrt{A_5(r)}F}\{A_1(r)[2Mr + a^2 A_2(r)^2\sin^2\theta] - a^2 A_2(r)\sin^2\theta\},$$

$$g_{t\phi}^{\text{KS}} = -\frac{a\tilde{\Sigma}[(r^2 + a^2)A_1(r)A_2(r) - \Delta]\sin^2\theta}{F},$$

$$g_{rr}^{\text{KS}} = \frac{\tilde{\Sigma}A_1(r)}{A_5(r)F}\{A_1(r)[\Delta + 4Mr + a^2 A_2(r)^2\sin^2\theta] - 2a^2 A_2(r)\sin^2\theta\},$$

$$g_{r\phi}^{\text{KS}} = -\frac{a\tilde{\Sigma}\sin^2\theta}{\sqrt{A_5(r)}F}[(r^2 + a^2)A_1(r)^2 A_2(r) + 2MrA_1(r) - a^2 A_2(r)\sin^2\theta],$$

$$g_{\theta\theta}^{\text{KS}} = \tilde{\Sigma},$$

$$g_{\phi\phi}^{\text{KS}} = \frac{\tilde{\Sigma}[(r^2 + a^2)^2 A_1(r)^2 - a^2\Delta\sin^2\theta]\sin^2\theta}{F}, \qquad (1)$$

where

$$F \equiv [(r^2 + a^2)A_1(r) - a^2 A_2(r)\sin^2\theta]^2.$$

B. The HARMPI code

As mentioned in the Introduction, there are several GRMHD codes that are able to construct and evolve accretion disks around BHs. Many of them can be seen in Ref. [41], where a direct comparison between them is examined.

The starting point for the code used in this work is HARMPI [21]. This is a public, parallelized, three-dimensional version of HARM [18,19], one of the first GRMHD codes to be developed. It has been chosen for its accessibility, parallelization and recent release date. Apart from it there are a handful of branches from the initial code worth mentioning here. A primary derivative is iHARM3d where the equations are solved on a Cartesian grid in arbitrary coordinates and the fluxes are calculated using the local Lax-Friedrichs (LLF) method (Ref. [42]). A recent version is H-AMR, extensively updated with improved performance as the main goal, and some new features [43,44]. Another widely used version is HARM-Noble, or HARM3D [20,45]. It is a variant similar to iHARM with several modest changes, like the incorporation of agnostic coordinates and spacetime choices, making it in a way generally covariant. Lastly, there is rHARM (Ref. [46]) with two new physical parameters that have been added to the system, electric field variable and resistivity (or magnetic diffusivity), serving the purpose of smoother, more organic jets evolution.

In its core, HARM solves hyperbolic partial differential equations in conservative form using high-resolution, shock-capturing techniques. It has been configured with

the purpose of solving the relativistic magnetohydrodynamic equations of motion in a stationary black hole spacetime in Kerr-Schild coordinates, with the goal to evolve an accreting disk. These are (as in e.g., Ref. [20]) the continuity equation

$$\nabla_\mu(\rho u^\mu) = 0, \tag{2}$$

the equation of local energy conservation

$$\nabla_\mu T^\mu_\nu = 0, \tag{3}$$

and Maxwell's equations

$$\nabla_\nu F^{\star\mu\nu} = 0, \tag{4}$$

$$\nabla_\nu F^{\mu\nu} = J^\mu. \tag{5}$$

Where, ρ is the rest-mass density, u^μ is the 4-velocity of the fluid, $F^{\mu\nu}$ is the Faraday tensor times $1/\sqrt{4\pi}$, $F^{\star\mu\nu}$ is the dual of this tensor or the Maxwell tensor times $1/\sqrt{4\pi}$, and J^μ is the 4-current. In a flux conservative form the equations can be expressed as

$$\partial_t \mathcal{U}(P) = -\partial_i \mathcal{F}^i(P) + \mathcal{S}(P), \tag{6}$$

where $\mathcal{U}$ is a vector of "conserved" variables, F^i are the fluxes, and S is a vector of source terms. Explicitly these are

$$\mathcal{U}(P) = \sqrt{-g}[\rho u^t, T^t_t + \rho u^t, T^t_j, B^k]^T \tag{7}$$

$$\mathcal{F}^i(P) = \sqrt{-g}[\rho u^i, T^i_t + \rho u^i, T^i_j, (b^i u^k - b^k u^i)]^T \tag{8}$$

$$\mathcal{S}(P) = \sqrt{-g}[0, T^\kappa_\lambda \Gamma^\lambda_{t\kappa}, T^\kappa_\lambda \Gamma^\lambda_{j\kappa}, 0]^T, \tag{9}$$

where g is the determinant of the metric, $\Gamma^\lambda_{\mu\kappa}$ is the metric's affine connection, and $B^i = F^{*it}$ is our magnetic field.

The total stress-energy tensor is the sum of the fluid part,

$$T^{\mu\nu}_{\text{fluid}} = \rho h u^\mu u^\nu + P g^{\mu\nu}, \tag{10}$$

and the electromagnetic part

$$\begin{aligned} T^{\mu\nu}_{\text{EM}} &= F^{\mu\lambda} F^\nu_\lambda - \frac{1}{4} g^{\mu\nu} F^{\kappa\lambda} F_{\lambda\kappa} \\ &= |b|^2 u^\mu u^\nu + \frac{1}{2}|b|^2 g^{\mu\nu} - b^\mu b^\nu, \end{aligned} \tag{11}$$

where $g_{\mu\mu}$ is the metric, $h = (1 + \epsilon + P/\rho)$ is the specific enthalpy, P is the pressure, ϵ is the specific internal energy density (note the difference with the deformation parameter ϵ_3), $b^\mu = F^{*\nu\mu} u_\nu$ is the magnetic field 4-vector, and $|b|^2 \equiv b^\mu b_\mu$ is twice the magnetic pressure.

The equations of motion are closed by an equation of state, $P = (\Gamma - 1)\rho\epsilon$ or $P = K\rho^\gamma$, where Γ is the adiabatic index, and K is the entropy parameter.

III. MODEL

In order to model a thin disk around a Johannsen BH, we had to implement three major extensions (or alterations) to the initial package of HARMPI. We had to add the metric functions describing the Johannsen metric, we had to implement a cooling function, so that we can dictate the geometric thickness of the disk and we had to change the initial disk profile, so that it matches the literature that we followed.

The change of metric is fairly straight forward. We defined globally the parameters ϵ_3, α_{13}, α_{22}, α_{52} and we wrote the functions to calculate the metric components in both BL and KS coordinates. Then, we interchanged all previous metric functions with our own. When all parameters are zero, the metric gets simplified to the Kerr metric. With this modification, HARMPI operates on a deformed spacetime.

A. Cooling function

As discussed before, HARMPI solves equations in a flux conservative form, meaning that the energy dissipated by the turbulent effects of the fluid remains in the fluid in the form of heat. Thus, without the introduction of a loss term in the energy equation, the disk would constantly get hotter and thicker. Eventually the thermal energy would get captured by the hole or carried away by winds. Since we are interested in the thin disk case, it is essential to release this heat.

To accomplish efficient cooling, we implement a cooling function, following the work of Ref. [20]. First, we define vertical thickness. There are a few ways to calculate it; in this work we use the vertical density moment, as it does not need the assumption of a Gaussian profile:

$$H(r) = \frac{\int d\theta d\phi \sqrt{-g}\sqrt{g_{\theta\theta}}\rho|\theta - \pi/2|}{\int d\theta d\phi \sqrt{-g}\rho}. \tag{12}$$

Often, we will use the variable $\tilde{H} = H/r$ instead of H. The temperature of the disk that should produce a desired aspect ratio H/r in Newtonian gravity is

$$T_* = \frac{\pi}{2}\left[\frac{H}{r} r\Omega(r)\right]^2. \tag{13}$$

For $\Omega(r)$ we use the angular velocity of a particle in a circular orbit in the equatorial plane [28],

$$\Omega(r) = \frac{-\partial_r g_{t\phi} + \sqrt{(\partial_r g_{t\phi})^2 - \partial_r g_{\phi\phi} \partial_r g_{tt}}}{\partial_r g_{\phi\phi}}. \tag{14}$$

This choice serves two purposes. First, it is the fully relativistic expression of $\Omega(r)$ for equatorial circular geodesics around a non-Kerr BH and includes the contribution from deformation parameters. Second, when deformation parameters equal zero, it matches the relativistic Keplerian frequency expression used in literature [20], allowing for a comparison of results in the Kerr limit. For radii smaller than ISCO, we use $\Omega(r_{\mathrm{ISCO}})$ in Eq. (13).

The cooling function $\mathcal{L}$, which is basically the rate at which energy is radiated per unit proper time in the fluid frame, is defined as

$$\mathcal{L} = s\Omega\rho\epsilon[Y - 1 + |Y - 1|]^q, \qquad (15)$$

where $Y = (\Gamma - 1)\epsilon/T_*$, $s = 1$ is a factor of proportionality and $q = 0.5$ dictates how fast the cooling acts when the fluid is above the desired temperature (T_*). Note how the absolute value of $(Y - 1)$ acts as a switch, turning off cooling whenever the fluid's temperature is below T_*. The free parameters were set to their default values, following Ref. [20].

To express the radiation we assume that it is isotropic in the fluid's frame, and so F_ν, the amount of radiated energy-momentum per unit 4-volume in the coordinate frame is

$$F_\nu = \mathcal{L}u_\nu. \qquad (16)$$

Finally, we use their assumption, that the radiation described by this loss term acts in all the volume of the disk, and so the local energy conservation equation reads

$$\nabla_\mu T^\mu_\nu = -F_\nu. \qquad (17)$$

With this equation the procedure is complete and can be summarized as follows. First, we set the desired aspect H/r and we calculate the temperature T_* that would keep a disk at this thickness. We construct the cooling function $\mathcal{L}$, and we implant it in the local energy conservation equation.

B. Initial disk profile

In principle, the initial disk profile should be irrelevant for the final thin disk profile we are simulating. However, in practice, this is not established and is an active area of research [47,48]. We change the default initial disk profile in the original version of HARMPI, taken from Ref. [49], to the one used more often in literature (e.g., in Refs. [20,45,50–56]), given in Ref. [37]. The first benefit from this is that the initial disk is a bit thinner ($\tilde{H}_{\mathrm{max}} \sim 0.28$ in the case of Ref. [37] vs $\tilde{H}_{\mathrm{max}} \sim 0.35$ in the case of Ref. [49]), where $\tilde{H}_{\mathrm{max}}$ is the maximum value of $\tilde{H}$ along the disk's surface). More importantly, it is easier for us to compare our results with the literature. We now discuss this initial disk profile, following the notation of Ref. [50].

The starting point of this idea is a solution where the angular velocity in the disk has a power law form

$$\Omega = \eta\lambda^{-q}, \qquad (18)$$

where η is a constant, q is a positive parameter, and λ is given by

$$\lambda^2 = \frac{l}{\Omega} = l\frac{g^{tt} - lg^{t\phi}}{g^{t\phi} - lg^{\phi\phi}}. \qquad (19)$$

It is easy to show that λ is the cylindrical radius in Newtonian gravity, i.e., $\lambda = r\sin\theta$. Note, that l and Ω are defined as

$$l = -\frac{u_\phi}{u_t}; \quad \Omega = \frac{u^\phi}{u^t}. \qquad (20)$$

We start with the equation of momentum evolution in the hydrodynamic limit, with the assumptions of time independence, axisymmetry and no poloidal motion,

$$\frac{\partial_j(P)}{\rho h} = -\frac{u_t^2}{2}\partial_j(u_t^{-2}) + u_t^2(-\partial_j g^{t\phi} + l\partial_j g^{t\phi})\partial_j l, \qquad (21)$$

where P is the pressure, h is the specific enthalpy and $u_t^{-2} = g^{tt} - 2lg^{t\phi} + l^2 g^{\phi\phi}$, a result which follows from $u_\mu u^\mu = -1$, considering $u_r = u_\theta = 0$.

Furthermore, by imposing constant entropy, i.e., $TdS = 0$, and using $dh = dp/\rho$, it follows that

$$\frac{\partial_j h}{h} = -\frac{1}{2}\frac{\partial_j(u_t^{-2})}{u_t^{-2}} + u_t^2(-\partial_j g^{t\phi} + l\partial_j g^{t\phi})\partial_j l. \qquad (22)$$

The next step is to integrate this equation, and for simplicity the assumption $\Omega \equiv \Omega(l)$ is used, along with the relation $\Omega = (g^{t\phi} - lg^{\phi\phi})/(g^{tt} - lg^{t\phi})$. The expressions for l and Ω can be rewritten as

$$l = \eta\lambda^{2-q}; \quad \Omega = \eta^{-2/(q-2)}l^{q/(q-2)} \equiv kl^\alpha, \qquad (23)$$

where $\alpha = q/(q - 2)$. A general solution arises when setting enthalpy at the inner edge of the disk to zero ($h_{\mathrm{in}} = 0$) and determining the surface binding energy u_{in}

$$h(r, \theta) = \frac{u_{\mathrm{in}}f(l_{\mathrm{in}})}{u_t(r, \theta)f(l(r, \theta))}, \qquad (24)$$

where

$$f(l) = |1 - kl^{(a+1)}|^{1/(a+1)}. \qquad (25)$$

Using the equation of state and the definition of enthalpy, the internal energy of the disk is

$$\epsilon(r, \theta) = \frac{1}{\Gamma}\left\{\frac{u_{\mathrm{in}}f(l_{\mathrm{in}})}{u_t(r, \theta)f(l(r, \theta))} - 1\right\}, \qquad (26)$$

and the density

$$\rho = [\epsilon(\Gamma - 1)/\kappa]^{1/(\Gamma-1)}.$$

The surface binding energy u_{in} can be explicitly defined if we provide l_{in}. Lastly, we provide a way to calculate η (or k). We make use of

$$\frac{l}{l_{\text{in}}} = \left(\frac{\lambda}{\lambda_{\text{in}}}\right)^{2-q}, \qquad (27)$$

so it follows that

$$\eta = \frac{l_{\text{in}}}{(\lambda_{\text{in}})^{2-q}}; \quad k = \eta^{-2/q-2}. \qquad (28)$$

Eventually, we can calculate enthalpy (h) at any point of the disk, and subsequently ρ, as well as the components u_t, u_ϕ of the 4-velocity, which gives us the complete profile of the disk.

IV. SIMULATION PARAMETERS

In our effort to explore the effect that deformation parameters bring to the models as broadly as possible, we use various combinations of parameters. Some of our simulations are in pure Kerr background, which serve as benchmark.

The simulations reported here are 2D that use a 192×192 grid in the radial and polar directions, with $r \in [\sim R_{\text{hor}}, 120]$, and $\theta \in [0.05\pi, 0.95\pi]$. To check for convergence we run simulations both with higher and lower resolutions and the chosen configuration was the optimal combination of resolution and computational time. We also run a 3D model with resolution $96 \times 96 \times 64$, but computationally, it was too expensive for the number of simulations that we performed (taking on average a 100 times longer than the 2D simulations). The details of the 3D case are presented in Appendix.

We set the inner edge of the initial disk to $R_{\text{in}} = 15M$ and the parameter $q = 1.68$. The specific angular momentum l_{in} was adjusted differently in every case (exact values given in Table I) to result always in a similar disk with the same pressure maximum point $R_{\text{pmax}} = 25$. Figure 1 shows the initial disk profile, identical to the solution of Ref. [37] and same for all cases.

The adiabatic index, and the entropy parameter are set to $\Gamma = 5/3$ and $K = 0.01$. The parameter β, defined as the ratio of the gas pressure to the magnetic pressure, using the volume-integrated gas pressure divided by the volume-integrated magnetic energy density in the initial torus, was set equal to 100. The desired thickness was set to $\tilde{H}_d = (H/r)_{\text{desired}} = 0.12$. We control the discretization of the grid through the parameter $h_{\text{KMS}} = 0.3$, that produces smaller cells as the radius gets smaller and the closer we are at the equatorial plane. The floor for the background

TABLE I. List of all the simulations discussed in the text. Deformation parameters when not mentioned are set to zero. Spin and ISCO are in given in units of M and the values for mass are given in code units.

Case	Spin	Non-Kerr Parameter	ISCO	l_{in}	M
I	0.9	0	2.32	4.58	30500
II	0.678	$a_{13} = -2$	2.32	4.61	35000
III	0.9	$a_{52} = 3$	2.32	4.58	30500
IV	0.976	0	1.66	4.58	35200
V	0.9	$a_{13} = -1.5$	1.66	4.58	30500
VI	0.998	0	1.237	4.576	34000
IX$_{\text{3D}}$	0.9	0	2.32	4.58	18600

density has been set at $\rho_{\text{floor}} = 10^{-7}$. Turbulence was seeded by adding random perturbations to u at the 1% level. All simulations were evolved for $t = [0, 15000M]$, and we recorded the state of the disk every $t = 20M$.

Tab. I lists a subset of simulations we performed and those we will discuss in the rest of the paper. Our choices are driven by the anticipation, based on previous analyses of x-ray reflection spectroscopy, that there exists a degeneracy between BH spin and deformation parameters based on the size of ISCO. Thus, ISCO provides a measure of the BH field strength and a rubric for constructing the simulation set. We simulate cases with moderate ISCO radii (cases I, II, III) representing a BH neighborhood with moderately strong fields, and cases with very small ISCO radii (cases IV, V, VI) representing neighborhoods with extremely strong gravitational fields. From now, the simulations will be referred to using the case number from Table I.

V. RESULTS

A. Disk properties

In this first section of our results, we examine some fundamental properties of GRMHD disks regarding their
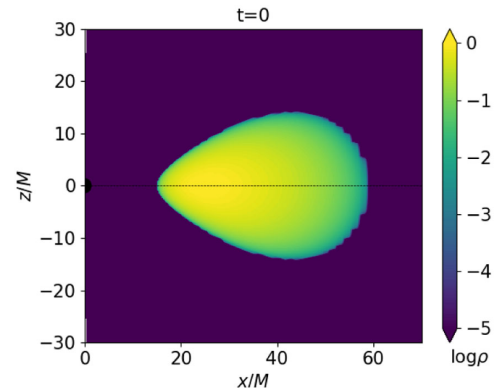

FIG. 1. A snapshot of the initial disk profile from a Kerr BH with $a = 0.9$. The density is in code units, normalized to 1. The black dashed line denotes the equatorial plane.
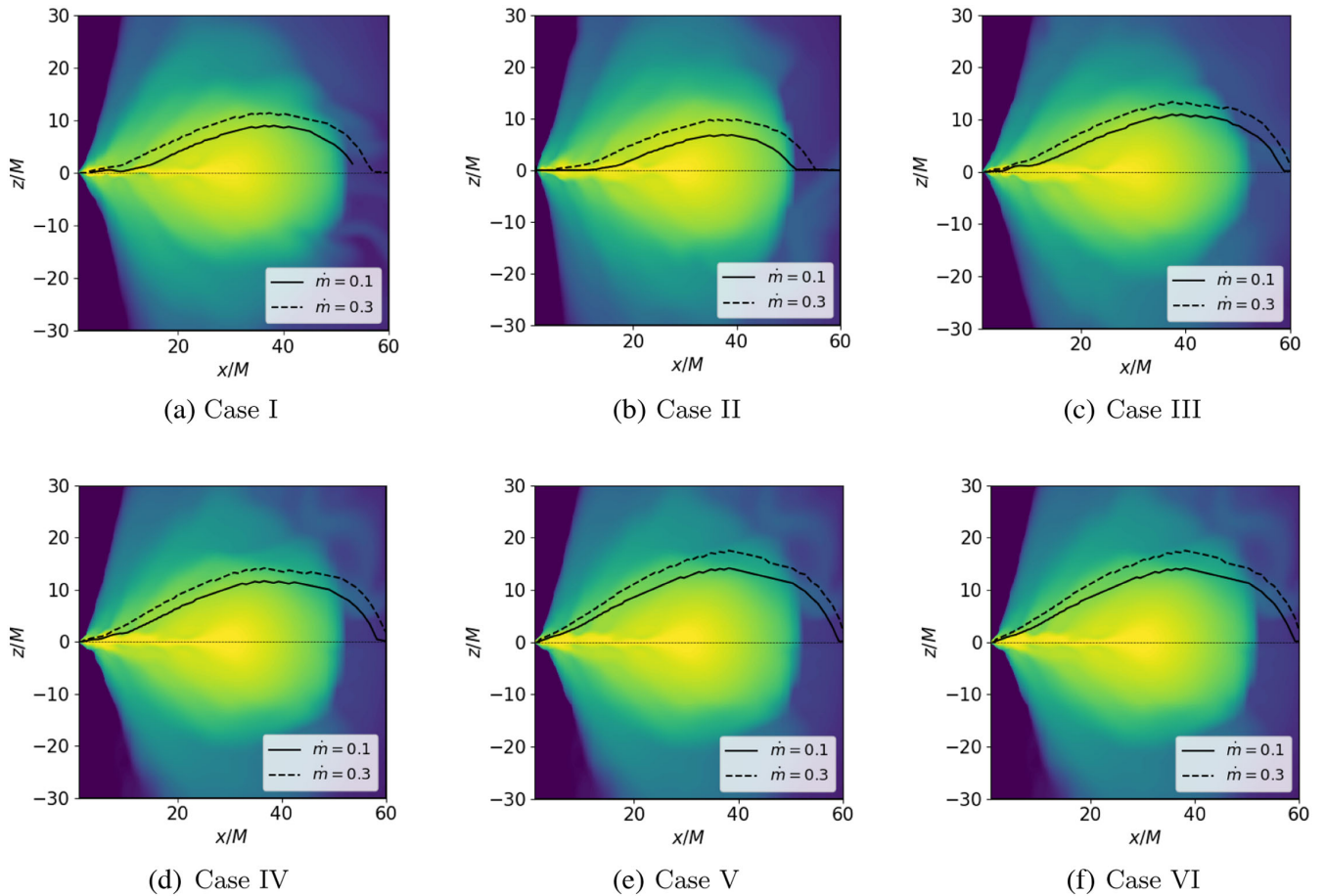
FIG. 2. Snapshots of the disk at the end of the simulation ($t = 15000M$) for different cases. The color coding remains the same as in Fig. 1. The solid and dashed black lines mark the time averaged height ($\tilde{H}_{\mathrm{ph}}$) of the surface of constant optical depth $\tau = 1$ for two indicative values of $\dot{m}$, and the dotted black line marks the equator. See text for more details.

structure and stability. Ensuring that the disks pass these first tests is essential for the credibility of the more complex calculations to follow.

In Fig. 2 we exhibit the disk at the last time frame from every simulation (the black overplotted lines are discussed in a later section). This is a typical image of a stable thin

accretion disk in stability. The disks reach stability around $t = 6000–8000M$ and remain stable till the end of the simulation. This is why all averaging is taking place in the interval $t = 8000–15000M$.

Next, in Fig. 3, we show profiles of the magnetic and gas pressure from case I. We can observe the thermal gas
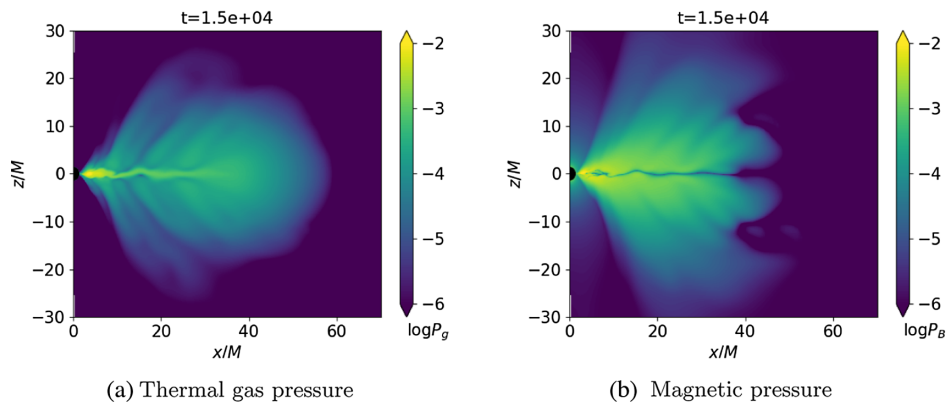

FIG. 3. Snapshots from case I of the magnetic and thermal gas pressure. The images were taken at the end of the simulation ($t = 15000M$).
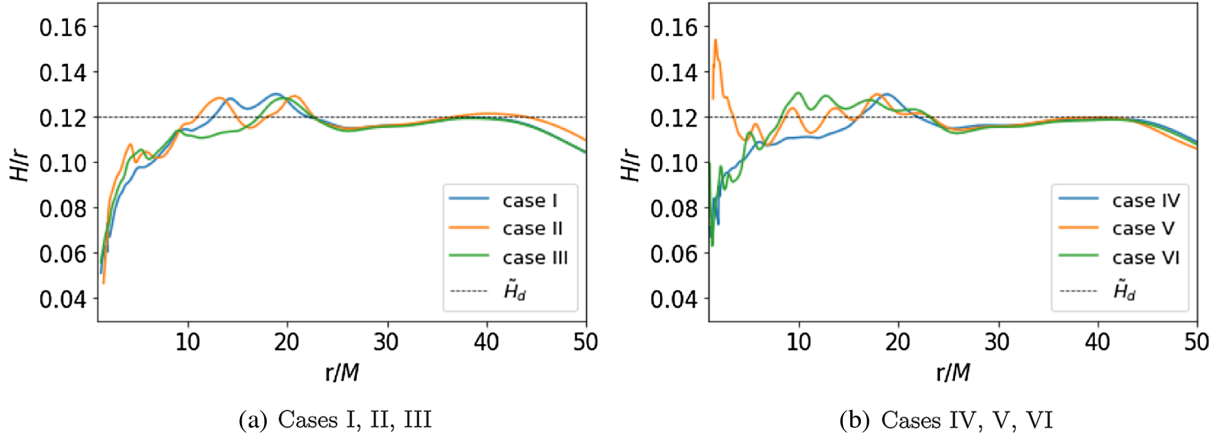
FIG. 4. Vertical thickness H/r, averaged over $t = 8000M - 15000M$, with respect to r. $\tilde{H}_d$ denotes the intended thickness ($= 0.12$).

pressure P_g having a similar behavior to the density ρ, peaking in the equatorial region. The magnetic pressure P_B, on the other hand, is practically zero in this region and reaches its maximum in an area very close to the hole (where the density of magnetic lines is larger), where both the gas and magnetic pressures are high.

In Fig. 4 we calculate the vertical thickness H/r as defined in Eq. (12). We conclude that in general, despite the different spins and deformation parameters, all models came very close to the goal ($\tilde{H}_d = 0.12$). This result is of great importance, as it shows that the simulated disks

indeed grew thinner, and the cooling function worked as intended. In case V there is a unique feature of the thickness rising sharply in the inner region of the disk. We discuss this case further below.

The next graphs are devoted to the stability of the disks. We test this by examining the behavior of the accretion rate both with respect to radius and time. We claim that the disks are in a steady state after $t = 8000M$, meaning that we expect a stable accretion. For the accretion as a function of time the fluctuations are unavoidable with any numerical approach, since the sampling is far from smooth. In Fig. 5,
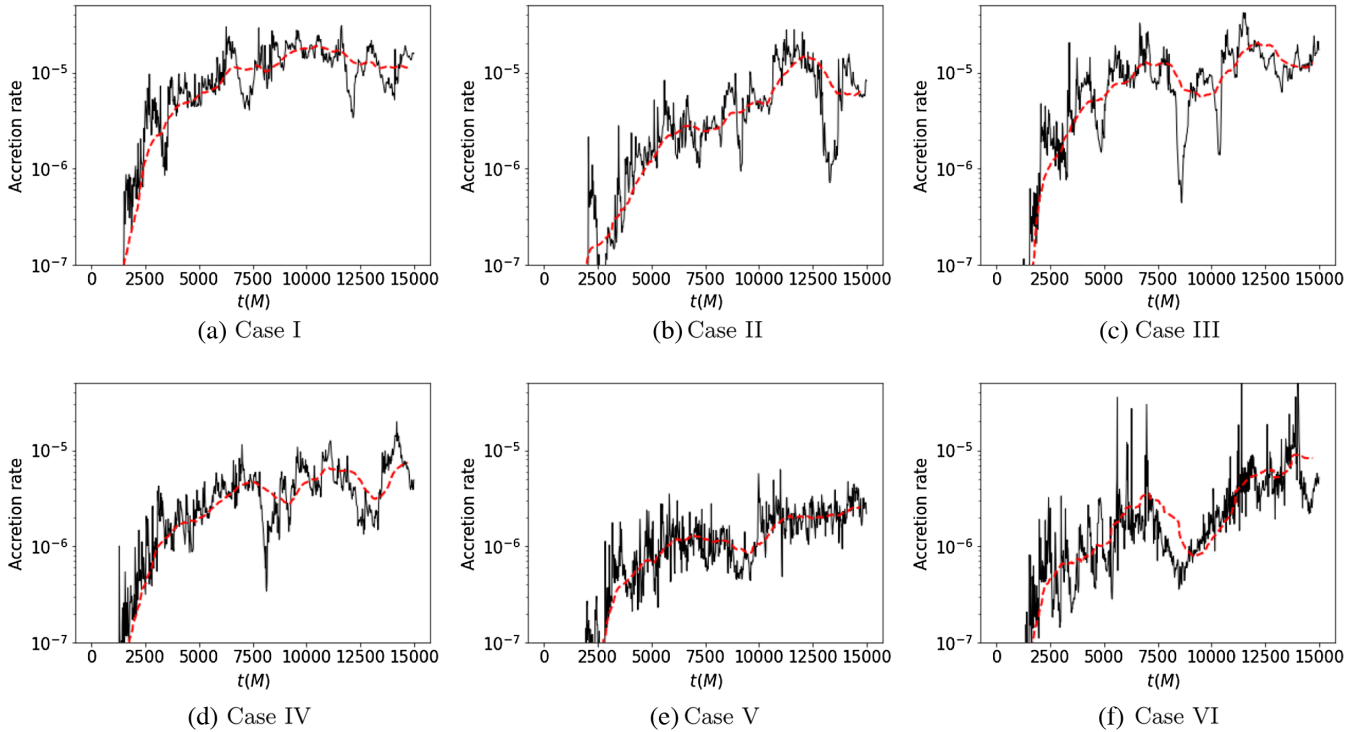

FIG. 5. Accretion rate at the horizon, in units of M_{code}/M, as a function of time for different cases. The red dashed line denotes the rolling average.
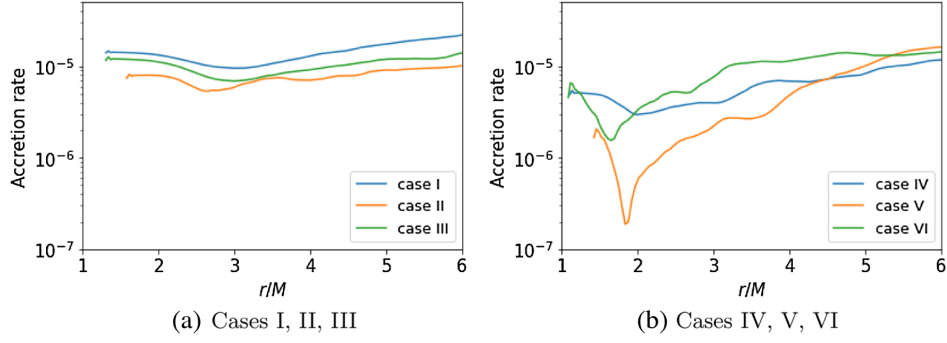
FIG. 6. Time averaged accretion rate, in units of M_{code}/M and averaged over $t = 8000M - 15000M$, with respect to r.

we present the accretion rate at the horizon, $\dot{M}(r_{\text{hor}})$, with respect to time. We can see that the accretion rate has stabilized and remains quite low. These graphs are similar to what is seen in typical GRMHD simulations (see, for instance, Fig. 14 from Ref. [24,50] as well as Fig. 1 from Ref. [54]).

In Fig. 6, the graphs of accretion (averaged in time) with respect to r are shown. The accretion rate is calculated as

$$\dot{M}(r) = \int_{2H} \int_{\phi} \rho(r,\theta,\phi) u^r(r,\theta,\phi) g_{\text{det}}(r,\theta,\phi)/M_{\text{code}},$$

(29)

where M_{code} is the mass of the disk in code units. For cases I-IV and VI, the rate stays in a close range to the value at the horizon. In case V though, there is a significant drop close to the ISCO. In fact, the drop in accretion rate seen here happens at similar radii where we saw a rise in thickness in Fig. 4. One possible explanation for this feature is the dampening of magnetorotational instabilities (MRIs) that can lead to a halt in accretion, which can occur especially in 2D simulations. Another possibility is the extreme nature of the parameter choice in this case: $a_* = 0.9$ and $\alpha_{13} = -1.5$ lies very close to the region of the parameter space where pathologies appear in the spacetime (for instance, naked singularities, see Fig. 6 in Ref. [38]).

B. Radiative efficiency

After establishing that the disk evolves as intended in a stable fashion and achieves the desired thickness, we turn our attention to observables. There are different ways to measure the radiation from a GRMHD disk. The first one, and most straight forward, is to consider the radiation produced from the cooling function $\mathcal{L}$, as described in section III A. Apart from giving us a way to control the vertical thickness, the function provides a self-consistent way of comparing emission from the simulated disk with that expected in a standard NT model. For doing so, we use the angle-averaged, fluid-frame luminosity per unit area, as in Ref. [20],

$$F_{\text{ff}}(r) = \frac{\int \int dx^{(\phi)} dx^{(\theta)} \mathcal{L}}{\int dx^{(\phi)}|_{\theta=\pi/2}},$$

(30)

where each component of the vector $dx^{(\mu)} = e_{\nu}^{(\mu)} dx^{\nu}$ represents the extent of a cell's dimension as measured in the fluid element's rest frame, and $e_{\nu}^{(\mu)}$ is the orthonormal tetrad that transforms vectors in the Boyer-Lindquist coordinate frame to the local fluid frame (see, e.g., Ref. [57], for explicit expressions of the tetrad). The vector dx^{ν} is the Boyer-Lindquist coordinate frame version of the Kerr-Schild vector $dx_{\text{KS}}^{\nu} = [0, \Delta r, \Delta\theta, \Delta\phi](r,\theta,\phi)$, where $\Delta r, \Delta\theta, \Delta\phi$ are the radial, poloidal, and azimuthal extents of our simulation's finite volume cell located at (r,θ,ϕ). Eventually, for a 2D simulation the radiated flux per unit area in the fluid frame is given as,

$$F(r) = \frac{\dot{M}}{\dot{M}(r)} \int \int (e_1^3 \Delta r + e_2^3 \Delta\theta)(e_1^2 \Delta r + e_2^2 \Delta\theta)\mathcal{L}. \quad (31)$$

We have inserted the factor $\dot{M}/\dot{M}(r)$ to compensate for any anomalies from the accretion rate. The flux for the NT model can be calculated as,

$$F_{\text{NT}}(r) = \frac{\dot{m}}{4\pi g} \frac{\partial_r \Omega}{(E - \Omega L)^2} \int_{r_{\text{isco}}}^{r} (E - \Omega L) \partial_r L \, dr, \quad (32)$$

where E stands for specific energy, L for specific angular momentum and Ω for the angular frequency. All quantities are considered in the equatorial plane, and can be calculated as,

$$\Omega = \frac{-\partial_r g_{t\phi} \pm \sqrt{(\partial_r g_{t\phi})^2 - (\partial_r g_{tt})(\partial_r g_{\phi\phi})}}{\partial_r g_{\phi\phi}}, \quad (33a)$$

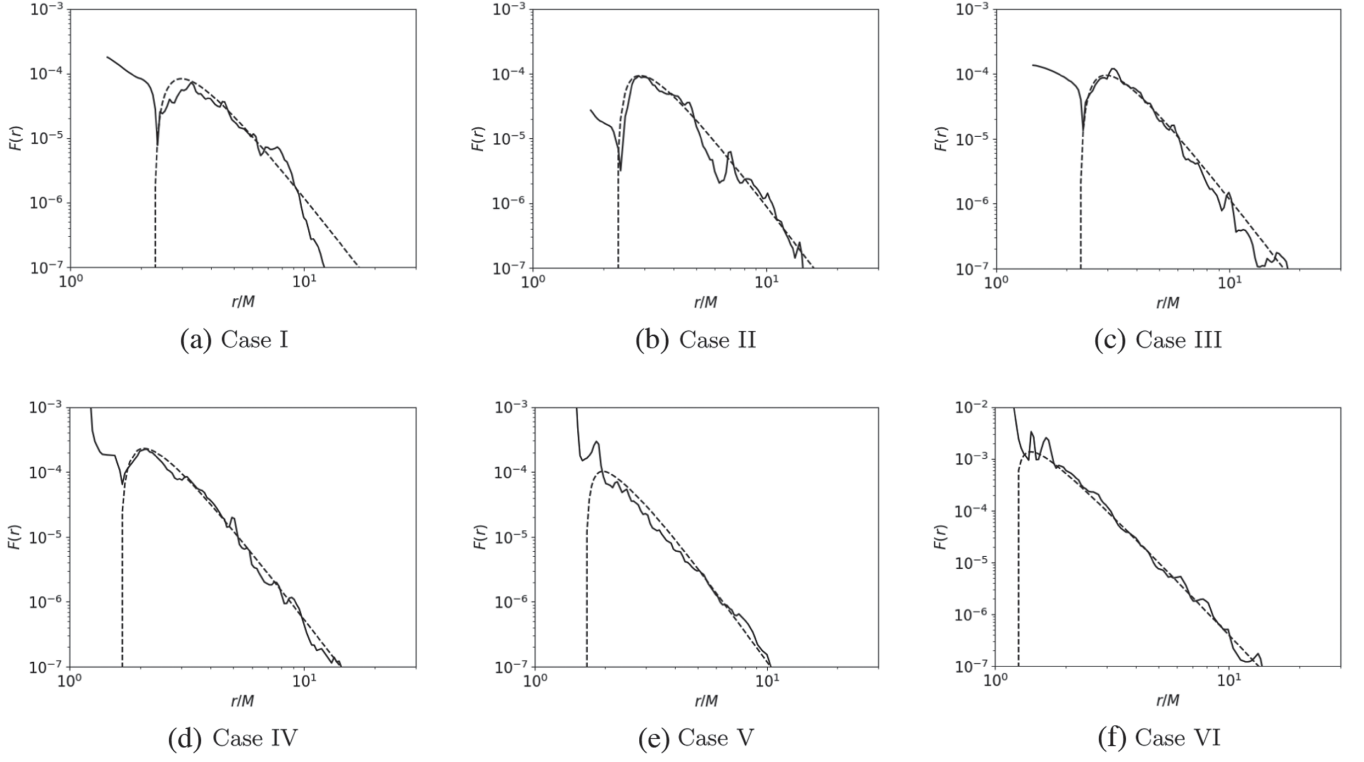$$E = -\frac{g_{tt} + \Omega_{t\phi}}{\sqrt{-g_{tt} - 2\Omega g_{t\phi} - \Omega^2 g_{\phi\phi}}}, \quad (33b)$$

(a) Case I (b) Case II (c) Case III

(d) Case IV (e) Case V (f) Case VI

FIG. 7.   Radiated flux per unit area in the fluid frame, averaged over $t = 8000M - 15000M$, as a function of radius r. The dashed line denotes the corresponding line as predicted from the NT model, and described in the text.

$$L = \frac{g_{t\phi} + \Omega g_{\phi\phi}}{\sqrt{-g_{tt} - 2\Omega g_{t\phi} - \Omega^2 g_{\phi\phi}}}. \qquad (33c)$$

Note that when we calculate the F_{NT} to match a case with non zero deformation, we use the deformed metric components to calculate the quantities necessary (Ω, L, E). The factor $\dot{m}$ in Eq. (32) is a scaling parameter and takes a value between 0.05 and 0.2.

In Fig. 7 we compare the calculated $F(r)$ from all cases with the predicted flux from the NT model. The flux overall looks in satisfying agreement with the NT model. This result is very important as it can vigorously verify the effective performance of the cooling function $\mathcal{L}$ and

ultimately the assumption of a NT disk for modelling radiation in general. Here again, we see a deviation from the norm in the inner regions in case V (and to a small extent, case VI).

In Fig. 8 we provide the luminosity received at infinity per unit radial coordinate (dL/dr), computed following the scheme outlined in Ref. [20], assuming no radiation arrives from inside the ISCO. We again see distinct behavior of case V (and to some extent case VI) compared to all other cases in the inner region, close to the ISCO. Thus, we conclude that the disk structure and radiation in extreme gravity (both pure Kerr with extreme spin and non-Kerr with parameter values near the edge) exhibits interesting features when simulated. We cannot rule out the possibility

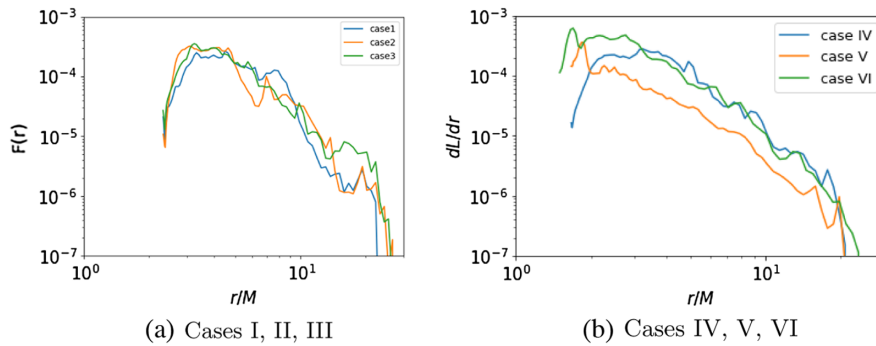(a) Cases I, II, III (b) Cases IV, V, VI

FIG. 8.   Luminosity received at infinity in different cases, based on radiated fluxes of Fig. 7. See the text for more details.

that these features are due to the 2D nature of the simulations, and assign a deeper investigation to a future work.

C. Reflection spectrum

We now discuss one of the simplest observables of x-ray reflection spectroscopy: the relativistically broadened iron line. It originates from those thermal photons that interact with, and get up-scattered by, coronal plasma, travel back toward the disk and get reflected. While the complete spectrum includes emission frequencies associated with all the elements (and their ionizations) present in the disk, the Kα emission of Iron dominates and for this reason is often the only part of the full reflection spectrum that is detected. For illustration, we therefore choose to present this single emission line. Though at the time of emission it is monochromatic, the motion of the disk, along with the motion of photons in the gravitational field of the BH, broadens it into a spectrum spread across a frequency band.

The first step in order to calculate the Fe Kα spectrum is to determine the reflecting surface, defined as $\tau = 1$, where τ is the optical depth. (We follow the notation of Refs. [53,55] for the calculation of the photosphere.) The optical depth can be calculated as

$$d\tau = \kappa \rho_{\mathrm{cgs}} r d\theta, \qquad (34)$$

where κ is the Thomson scattering opacity and ρ_{cgs} is the disk density in physical units, which can be calculated by relating it to the code density ρ_{code} as

$$\rho_{\mathrm{cgs}} = \rho_{\mathrm{code}} \frac{4\pi c^2}{\kappa G M} \frac{\dot{m}/\eta}{\dot{M}_{\mathrm{code}}}, \qquad (35)$$

where $\kappa = 0.4 \ \mathrm{cm^2 \, g^{-1}}$ is the electron scattering opacity, $\dot{m}$ is the Eddington-scaled accretion rate assuming a radiative efficiency $\eta = 0.06$ and M has been set to $10 \ M_\odot$. The photosphere is given by the following integral:

$$\int_{\theta=0}^{\Theta_{\mathrm{top}}} d\tau = 1, \qquad (36)$$

and the height of the photosphere is $H_{\mathrm{ph}} = r \cos \Theta_{\mathrm{top}}$. Note that θ starts from the z-axis, in essense $\theta \in (0, \pi)$. In Fig. 2 we show the photosphere for two values of $\dot{m}$, 0.1 and 0.3, for each simulation case. As expected, the height of the photosphere increases with the rate of Eddington-scaled accretion ($\dot{m}$), since higher accretion rate implies higher densities, and higher density reduces optical depth. The second variable that is able to make a difference in the height of the photosphere [Eqs. (35) and (36)] is the code's accretion rate ($\dot{M}_{\mathrm{code}}$). It is visible from the graphs that indeed cases with smaller accretion rates (namely, cases IV, V and VI, see Sec. VA) exhibit higher photospheres for both values of $\dot{m}$.

Having determined the location of the photosphere, we can now, in principle, raytrace photons from the photosphere to a far-away observer and compute the observed spectrum. Mathematically, following the notation of Ref. [28], the observed spectrum can be written as

$$F_{\mathrm{o}}(\nu_{\mathrm{o}}) = \int I_{\mathrm{o}}(\nu_{\mathrm{o}}, X, Y) d\tilde{\Omega}, \qquad (37)$$

where I_{o} is the specific intensity detected by the far-away observer, $d\tilde{\Omega} = dX dY/D^2$ is the element of the solid angle subtended by the disk's image in the observer plane, X and Y are the Cartesian coordinates of the disk's image in the same plane, and D is the distance between the observer and the point of emission. For computational convenience, what is done instead is to evolve the photons backwards in time from the observer to the point of emission, and to make use of a transfer function introduced in Ref. [58] and defined, following the notation of Ref. [28], as

$$f(g^*, r_{\mathrm{e}}, i) = \frac{1}{\pi r_{\mathrm{e}}} g \sqrt{g^*(1 - g^*)} \left| \frac{\partial(X, Y)}{\partial(g^*, r_{\mathrm{e}})} \right|, \qquad (38)$$

where r_{e} is the emission radius, i is the inclination of the observer relative to the BH spin axis,

$$g^* = \frac{g - g_{\mathrm{min}}}{g_{\mathrm{max}} - g_{\mathrm{min}}}, \qquad (39)$$

g is the redshift factor, defined as the ratio of photon frequencies at observation and emission, and g_{max} and g_{min} are the maximum and minimum values of g for a given r_{e} and i, respectively.

The equation for the spectrum looks like the following after the introduction of the transfer function:

$$F_{\mathrm{o}}(\nu_{\mathrm{o}}) = \frac{1}{D^2} \int_{r_{\mathrm{in}}}^{r_{\mathrm{out}}} \int_0^1 \pi r_{\mathrm{e}} \frac{g^2}{\sqrt{g^*(1 - g^*)}} \qquad (40)$$

$$\times f(g^*, r_{\mathrm{e}}, i) I_{\mathrm{e}}(\nu_{\mathrm{e}}, r_{\mathrm{e}}, \vartheta_{\mathrm{e}}) dg^* dr_{\mathrm{e}}. \qquad (41)$$

Here, I_{e} is the specific intensity at the point of emission. In principle, one could calculate this by analyzing the amount of thermal radiation being upscattered by the corona redirected toward the photosphere and reprocessed there, in a self-consistent manner (as done in, e.g., Ref. [55]). Another possibility is to raytrace photons from the corona, modeled as a point/line on the BH spin axis within the lamppost coronal geometry model [59], to the photosphere and reprocessed there. A third approach is to use a simple phenomenological intensity profile of a power-law (or a broken power-law). We follow the third approach and assume $I_{\mathrm{e}} \propto (r_e \sin \Theta_{\mathrm{top}})^{-3}$,. The calculation of the transfer function follows the scheme described in Ref. [28] with one important exception. In the present case, the reflecting
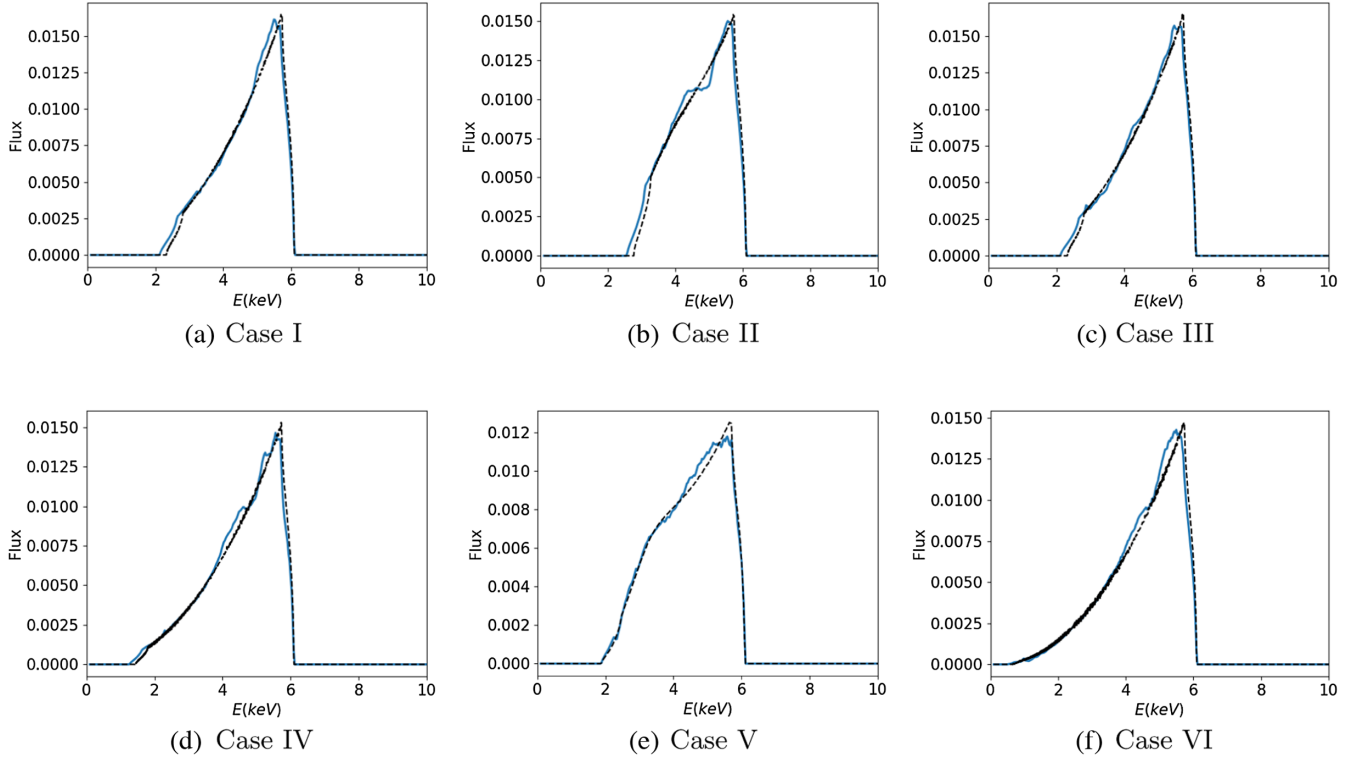
FIG. 9. Iron lines calculated for different cases. with $\dot{m} = 0.1$. The blue solid line is from simulations, and the black dotted line from the analytical Novikov-Thorne disk. See the text for more details.

surface does not always lie at the equator but at a certain height that depends on r_e. This dependence, moreover, is not analytical but only known numerically. We therefore implement an intersection function in the code that interpolates the disk surface using numerical data, identifies the step during evolution when this surface is crossed, and then interpolates the photon trajectory to determine the exact location where the photon would have hit the disk.

Following the above scheme, we calculate iron lines for each simulation listed in Table I, and these are plotted in Fig. 9. We assume the disk inner edge to lie at the ISCO radius and $\dot{m} = 0.1$ (results for $\dot{m} = 0.3$ show the same qualitative features). For each case, we also plot the iron lines for corresponding NT disks. In all cases, the agreement between the lines from the simulated disk and the NT disk, respectively, are excellent, minor fluctuations arising from numerical inaccuracies notwithstanding. The agreement occurs at both low and high spins, and for small and large non-zero deviations. Interestingly, the deviations from the NT model seen for cases V and VI in the previous sections are not present here. Indeed, when we plot H_{ph}/r, we find no spike in case V, unlike what we saw in plots of H/r.

The above serves to validate, on the one hand, the extended HARM code presented in this work and the additional framework to compute the reflection spectra described above, and, on the other hand, the NT-type disk

based RELXILL_NK suite for modelling the reflection spectra from accreting black holes with thin disks in the range of $\dot{m} \sim 0.1$–0.3. There is one last feature we note before closing this section. When looking at the radiated flux (Fig. 7) and luminosity (Fig. 8), we find negligible difference between cases I and II, representing moderately strong gravitational fields (especially in comparison with cases IV and V representing extremely strong gravitational fields). Whereas, their iron line plots are visibly distinct, bolstering the case for x-ray reflection spectroscopy as a sensitive test of deviations from the Kerr metric.

VI. FUTURE

With advances in observational tools and techniques, higher quality x-ray data is going to be available in the coming years and decades, enabling high quality reflection spectroscopy with accreting black holes, which will provide a versatile, independent from and complimentary to other techniques, and powerful tool to perform precision tests of gravity. Precise modeling of these astrophysical systems is therefore crucial. We present a first attempt in this direction with two and three dimensional simulations of the accretion disk around a non-Kerr object described by a theory-agnostic metric. The work makes several important strides in the path toward precise tests of gravity with high fidelity:

(a) We show that accreting matter evolves in a familiar pattern and settles into a typical disk for a non-GR BH metric, as compared to typical GR BH metrics (see Fig. 2 in comparison to [50,53], Figs. 5 and 6 in comparison to [54]).

(b) Radiated flux at source and luminosity are relatively weakly affected by deformations of the metric (being quite similar for cases I, II and III) as compared to the iron line.

(c) We validate the approximation of the accretion disk, with $\dot{m} \sim 0.1$–0.3, to a Novikov-Thorne type razor-thin disk for modelling the reflection spectra. This was shown to be valid in the Kerr case [47,48], and here we show it continues to remain valid in non-Kerr cases.

This work construes only a small step and there are many more improvements to be made in order for the framework to be of practical use:

(a) One of the first extensions would be to perform the analysis with three-dimensional MHD. Computational constraints restricted us from performing the complete analysis in 3D, however, as we show in the Appendix, the code is ready and able to perform 3D simulations.

(b) The metric we have used is quite generic, yet it covers a subset of all possible non-Kerr metrics in the market. Other metrics, with additional interesting properties like chaos [60], can be implemented in the framework to see whether new features appear in the MHD evolution.

(c) More precise evaluation of the reflection spectrum requires proper modelling of the corona, by tracking

thermal photons as they get reprocessed and radiated back to the disk, as done in Ref. [55,56] within GR.

APPENDIX: A 3D SIMULATION

Ideally, we would like to have carried out all simulations in a 3D configuration, but this was not possible due to computational constraints. Each 2D simulation (with resolution 192×192) on a 128 core cluster took ~ 12 hours to run, and simply adding a third dimension (with resolution N) would extend the runtime by more than N times. At the end, we did perform one simulation in 3D to make sure that the code is capable of running in 3D and to compare the results with the 2D simulations. Note that the resolution is halved in the (r, θ) directions than the 2D simulations, while the resolution in the azimuthal direction is set to 64 (i.e., $96 \times 96 \times 64$). On a 258 core cluster (double the size of the 2D simulation cluster), this
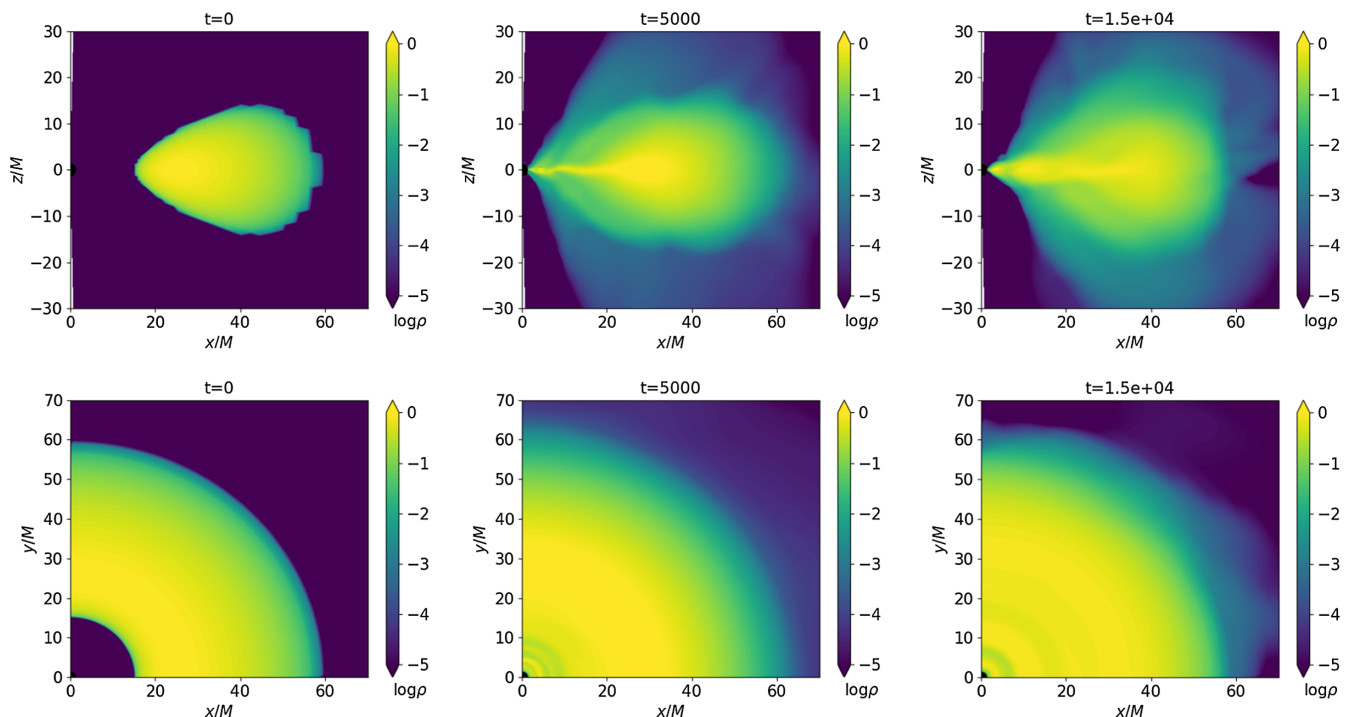

FIG. 10. Top: snapshots of the disk in the zx-plane, i.e., slicing at a constant azimuth. Bottom: screenshots of the disk evolution in the yx-plane, i.e., viewing the equatorial plane from top.
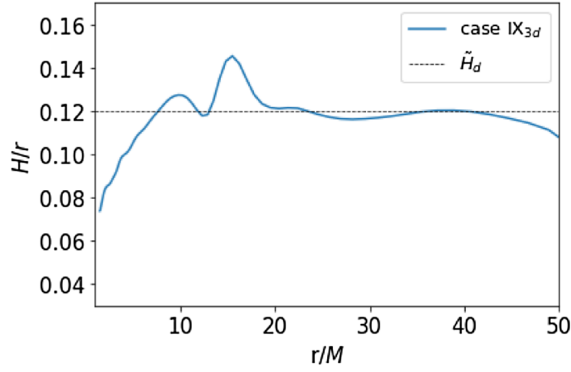
FIG. 11. Vertical thickness H/r, averaged over $t = 8000M - 15000M$, with respect to r. $\tilde{H}_d$ denotes the intended thickness (=0.12).
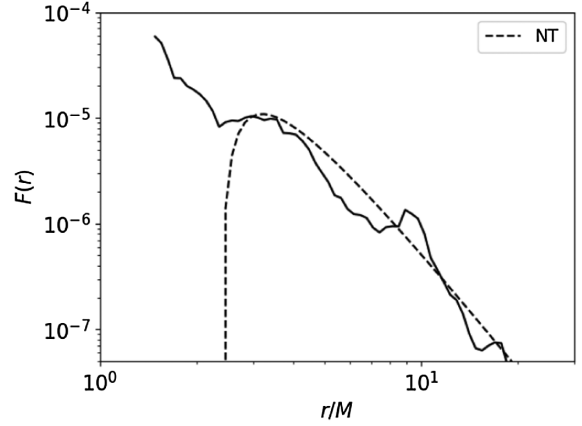

FIG. 13. Radiated flux per unit area in the fluid frame, averaged over $t = 8000M - 15000M$, as a function of radius r. The dashed line denotes the corresponding line as predicted from the NT model, and described in the text.

configuration took ∼10 days (20 times the 2D simulation runtime) to run.

The simulation parameters are listed in Table I under case 9_3D, and the results are shown in a series of plots in Figs. 10–13. Figure 10 shows the disk at various epochs (initial, intermediate, final). The initial disk is the same as in the 2D simulations (see Sec. III B for a description of the initial disk profile); in particular, it starts off independent of the azimuthal coordinate. Over time, the disk acquires a 3D profile, as can be seen in the bottom set of plots. Still, the 2D cross-section at a constant azimuth shows, in the top set of plots, a profile similar to the 2D simulations (cf. Fig. 2).

Figure 11 shows the vertical thickness H/r, which, as in the 2D simulations (Fig. 4), shows that desired thickness (0.12) was achieved. Figure 12 presents the accretion

rate, as a function of time (left panel) at the horizon and as a function of radius (right panel) averaged over $t = 8000M - 15000M$. In both cases, the accretion rate is along expected lines (cf. Figs. 5 and 6). In particular, note that the accretion rate in the 3D case has noticeably less oscillations than the 2D cases, a consequence of the higher accuracy provided by the third dimension. Finally, in Fig. 13 we show the radiated flux from the disk (cf. Fig. 7). Outside the ISCO, there is very good agreement between the flux calculated with the 3D simulation and the flux from the analytical model, as was the case with 2D simulations.
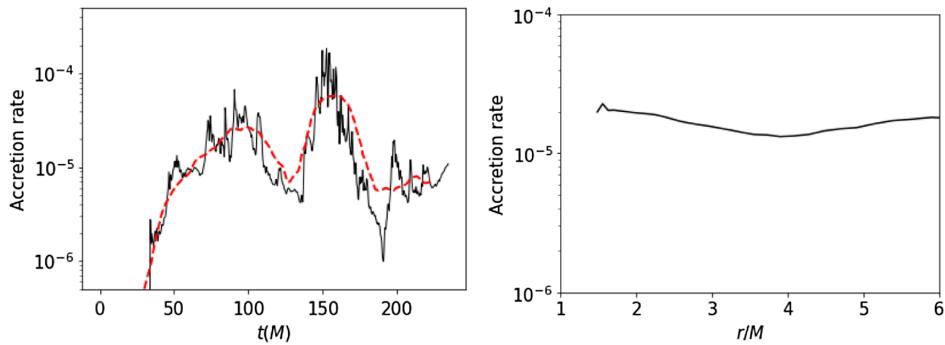

FIG. 12. Top: accretion rate at the horizon, as a function of time. The red dashed line denotes a rolling average. Bottom: time averaged accretion rate, in units of $M_{\rm code}/M$ and averaged over $t = 8000M - 15000M$, with respect to r.

[1] C. M. Will, Living Rev. Relativity **17**, 4 (2014).
[2] R. Abbott *et al.* (LIGO Scientific, Virgo, KAGRA Collaborations), arXiv:2112.06861.
[3] A. Tripathi, Y. Zhang, A. B. Abdikamalov, D. Ayzenberg, C. Bambi, J. Jiang, H. Liu, and M. Zhou, Astrophys. J. **913**, 79 (2021).
[4] R. Abuter *et al.* (GRAVITY Collaboration), Astron. Astrophys. **615**, L15 (2018).
[5] W. Israel, Phys. Rev. **164**, 1776 (1967).
[6] W. Israel, Commun. Math. Phys. **8**, 245 (1968).
[7] S. W. Hawking, Commun. Math. Phys. **25**, 152 (1972).
[8] D. C. Robinson, Phys. Rev. Lett. **34**, 905 (1975).
[9] O. D. Elbert, J. S. Bullock, and M. Kaplinghat, Mon. Not. R. Astron. Soc. **473**, 1186 (2018).
[10] B. P. Abbott *et al.* (LIGO Scientific, Virgo Collaborations), Phys. Rev. Lett. **116**, 221101 (2016); **121**, 129902(E) (2018).
[11] J. H. Taylor and J. M. Weisberg, Astrophys. J. **253**, 908 (1982).
[12] D. Psaltis, Living Rev. Relativity **11**, 9 (2008).
[13] Z. Cao, S. Nampalliwar, C. Bambi, T. Dauser, and J. A. Garcia, Phys. Rev. Lett. **120**, 051101 (2018).
[14] K. Akiyama *et al.* (Event Horizon Telescope Collaboration), Astrophys. J. Lett. **875**, L6 (2019).
[15] J. E. McClintock, R. Shafee, R. Narayan, R. A. Remillard, S. W. Davis, and L.-X. Li, Astrophys. J. **652**, 518 (2006).
[16] J. M. Bardeen and J. A. Petterson, Astrophys. J. Lett. **195**, L65 (1975).
[17] J. A. Font, Living Rev. Relativity **11**, 7 (2008).
[18] C. F. Gammie, J. C. McKinney, and G. Toth, Astrophys. J. **589**, 444 (2003).
[19] S. C. Noble, C. F. Gammie, J. C. McKinney, and L. Del Zanna, Astrophys. J. **641**, 626 (2006).
[20] S. C. Noble, J. H. Krolik, and J. F. Hawley, Astrophys. J. **692**, 411 (2009).
[21] A. Tchekhovskoy, Harmpi, https://github.com/atchekho/harmpi (2019).
[22] J. C. McKinney, A. Tchekhovskoy, A. Sadowski, and R. Narayan, Mon. Not. R. Astron. Soc. **441**, 3177 (2014).
[23] M. Liska, K. Chatterjee, A. Tchekhovskoy, D. Yoon, D. van Eijnatten, C. Hesp, S. Markoff, A. Ingram, and M. van der Klis, arXiv:1912.10192.
[24] O. Porth, H. Olivares, Y. Mizuno, Z. Younsi, L. Rezzolla, M. Moscibrodzka, H. Falcke, and M. Kramer, Comput. Astrophys. **4**, 1 (2017).
[25] H. Olivares, Z. Younsi, C. M. Fromm, M. De Laurentis, O. Porth, Y. Mizuno, H. Falcke, M. Kramer, and L. Rezzolla, Mon. Not. R. Astron. Soc. **497**, 521 (2020).
[26] Y. Mizuno, Z. Younsi, C. M. Fromm, O. Porth, M. De Laurentis, H. Olivares, H. Falcke, M. Kramer, and L. Rezzolla, Nat. Astron. **2**, 585 (2018).
[27] R. P. Kerr, Phys. Rev. Lett. **11**, 237 (1963).
[28] C. Bambi, A. Cardenas-Avendano, T. Dauser, J. A. Garcia, and S. Nampalliwar, Astrophys. J. **842**, 76 (2017).
[29] A. B. Abdikamalov, D. Ayzenberg, C. Bambi, T. Dauser, J. A. Garcia, and S. Nampalliwar, Astrophys. J. **878**, 91 (2019).

[30] Y. Zhang, A. B. Abdikamalov, D. Ayzenberg, C. Bambi, T. Dauser, J. A. Garcia, and S. Nampalliwar, Astrophys. J. **875**, 41 (2019).
[31] Y. Xu, S. Nampalliwar, A. B. Abdikamalov, D. Ayzenberg, C. Bambi, T. Dauser, J. A. Garcia, and J. Jiang, Astrophys. J. **865**, 134 (2018).
[32] Z. Yu, Q. Jiang, A. B. Abdikamalov, D. Ayzenberg, C. Bambi, H. Liu, S. Nampalliwar, and A. Tripathi, Phys. Rev. D **104**, 084035 (2021).
[33] K. Choudhury, S. Nampalliwar, A. B. Abdikamalov, D. Ayzenberg, C. Bambi, T. Dauser, and J. A. Garcia, Astrophys. J. **879**, 80 (2019).
[34] A. Tripathi, S. Nampalliwar, A. B. Abdikamalov, D. Ayzenberg, J. Jiang, and C. Bambi, Phys. Rev. D **98**, 023018 (2018).
[35] S. Nampalliwar, S. Xin, S. Srivastava, A. B. Abdikamalov, D. Ayzenberg, C. Bambi, T. Dauser, J. A. Garcia, and A. Tripathi, Phys. Rev. D **102**, 124071 (2020)..
[36] A. B. Abdikamalov, D. Ayzenberg, C. Bambi, S. Nampalliwar, and A. Tripathi, Phys. Rev. D **104**, 024058 (2021).
[37] S. K. Chakrabarti, Astrophys. J. **288**, 1 (1985).
[38] T. Johannsen, Phys. Rev. D **88**, 044002 (2013).
[39] B. Carter, Phys. Rev. Lett. **26**, 331 (1971).
[40] G. O. Papadopoulos and K. D. Kokkotas, Classical Quantum Gravity **35**, 185014 (2018).
[41] O. Porth *et al.* (Event Horizon Telescope Collaboration), Astrophys. J. Suppl. Ser. **243**, 26 (2019).
[42] V. Rusanov, Zh. Vychisl. Mat. Mat. Fiz. **1**, 267 (1961).
[43] M. Liska, A. Tchekhovskoy, and E. Quataert, Mon. Notes Astron. Soc. South. Afr. **494**, 3656 (2020).
[44] K. Chatterjee, M. Liska, A. Tchekhovskoy, and S. B. Markoff, Mon. Not. R. Astron. Soc. **490**, 2200 (2019).
[45] S. C. Noble, J. H. Krolik, J. D. Schnittman, and J. F. Hawley, Astrophys. J. **743**, 115 (2011).
[46] Q. Qian, C. Fendt, S. Noble, and M. Bugli, Astrophys. J. **834**, 29 (2017).
[47] R. F. Penna, J. C. McKinney, R. Narayan, A. Tchekhovskoy, R. Shafee, and J. E. McClintock, Mon. Not. R. Astron. Soc. **408**, 752 (2010).
[48] A. K. Kulkarni, R. F. Penna, R. V. Shcherbakov, J. F. Steiner, R. Narayan, A. Sadowski, Y. Zhu, J. E. McClintock, S. W. Davis, and J. C. McKinney, Mon. Not. R. Astron. Soc. **414**, 1183 (2011).
[49] L. G. Fishbone and V. Moncrief, Astrophys. J. **207**, 962 (1976).
[50] J.-P. D. Villiers, J. F. Hawley, and J. H. Krolik, Astrophys. J. **599**, 1238 (2003).
[51] R. Shafee, J. C. McKinney, R. Narayan, A. Tchekhovskoy, C. F. Gammie, and J. E. McClintock, Astrophys. J. Lett. **687**, L25 (2008).
[52] S. C. Noble, J. H. Krolik, and J. F. Hawley, Astrophys. J. **711**, 959 (2010).
[53] J. D. Schnittman, J. H. Krolik, and S. C. Noble, Astrophys. J. **769**, 156 (2013).
[54] J. D. Schnittman, J. H. Krolik, and S. C. Noble, Astrophys. J. **819**, 48 (2016).
[55] B. E. Kinch, J. D. Schnittman, T. R. Kallman, and J. H. Krolik, Astrophys. J. **826**, 52 (2016).

[56] B. E. Kinch, J. D. Schnittman, T. R. Kallman, and J. H. Krolik, Astrophys. J. **873,** 71 (2019).

[57] K. Beckwith, J. Hawley, and J. Krolik, Mon. Not. R. Astron. Soc. **390,** 21 (2008).

[58] C. T. Cunningham, Astrophys. J. **202,** 788 (1975).

[59] T. Dauser, J. Garcia, J. Wilms, M. Bock, L. W. Brenneman, M. Falanga, K. Fukumura, and C. S. Reynolds, Mon. Not. R. Astron. Soc. **430,** 1694 (2013).

[60] K. Destounis, A. G. Suvorov, and K. D. Kokkotas, Phys. Rev. Lett. **126,** 141102 (2021).